remote sensing

MDPI

Technical Note

Simulation of the Radar Cross Section of a Noctuid Moth

Freya I. Addison [1,†], Thomas Dally [2,†], Elizabeth J. Duncan [2], James Rouse [2], William L. Evans [1,2], Christopher Hassall [2] and Ryan R. Neely III [1,*]

[1] National Centre for Atmospheric Science and the School of Earth and Environment, University of Leeds, 71-75 Clarendon Rd., Woodhouse, Leeds LS2 9PH, UK; freya.addison@ncas.ac.uk (F.I.A.); w.l.evans@leeds.ac.uk (W.L.E.)

[2] School of Biology, Faculty of Biological Sciences, University of Leeds, Woodhouse Lane, Leeds LS2 9JT, UK; t.m.dally@leeds.ac.uk (T.D.); e.j.duncan@leeds.ac.uk (E.J.D.); j.l.rouse@leeds.ac.uk (J.R.); c.hassall@leeds.ac.uk (C.H.)

* Correspondence: r.neely@leeds.ac.uk; Tel.: +44-(0) 113-343-6417

† These authors contributed equally to this work.

Abstract: Electromagnetic modelling may be used as a tool for understanding the radar cross section (RCS) of volant animals. Here, we examine this emerging method in detail and delve deeper into the specifics of the modelling process for a single noctuid moth, with the hope of illuminating the importance of different aspects of the process by varying the morphometric and compositional properties of the model. This was accomplished by creating a high-fidelity three-dimensional insect model by micro-CT scanning a gold-palladium-coated insect. Electromagnetic simulations of the insect model were conducted by applying different morphological and compositional configurations using the WiPL-D Pro 3D Electromagnetic Solver. The simulation results show that high-resolution modelling of insects has advantages compared to the simple ellipsoidal models used in previous studies. We find that the inclusion of wings and separating the composition of the body, wings, and legs and antennae have an impact on the resulting RCS of the specimen. Such modifications to the RCS are missed when a prolate spheroid model is used and should not be ignored in future studies. Finally, this methodology has been shown to be useful in exploring the changes in the RCS that result from variations in specimen size. As such, utilising this methodology further for more species will improve the ability to quantitatively interpret aeroecological observations of weather surveillance radars and special-purpose entomological radars.

Keywords: radar cross section; insects; moths; radar; electromagnetic modelling

Citation: Addison, F.I.; Dally, T.; Duncan, E.J.; Rouse, J.; Evans, W.L.; Hassall, C.; Neely, R.R., III. Simulation of the Radar Cross Section of a Noctuid Moth. *Remote Sens.* **2022**, *14*, 1494. https://doi.org/10.3390/rs14061494

Academic Editor: Ali Khenchaf

Received: 12 February 2022
Accepted: 15 March 2022
Published: 20 March 2022

1. Introduction

The capability of weather surveillance radars (WSRs) to observe airborne organisms at regional and continental scales has been well known for over 70 years [1] and has given rise to a broad range of aeroecological research focusing predominately on birds [2–4], insects and bats [5–10] that utilise both traditional vertically pointing entomological radar as well as WSRs [10–14]. However, while it has been recognised that these observations can be used to detect insects, there remains a gap in our ability to use weather radar technology to observe volant animals, especially insects, in a quantitative context due to a lack of information about their radar cross sections (RCSs) [9,12,15,16].

The RCS of any object is a measure of the power density of the scattered electric field relative to that which was incident on the object [17]. As such, values of the RCS depend upon several inter-related parameters, including the shape, material (i.e., its dielectric constant), and size of the scatterer; the wavelength of the incident radiation; the incident and scattering angles of the radiation; and the polarization of the radiation with respect to the orientation of the scatterer [17,18]. If observations from dual-polarization WSRs are to

be fully exploited for ecological studies, precise RCS data, taking all these factors into consideration, are needed to interpret the observations [9,15,16,18]. This is especially true when ancillary data, such as trapping or visual data, are not available to help identify targets.

Direct measurements of the RCS of flying organisms, especially insects, are difficult to achieve, and it is not practical to collect the information necessary to interpret data documenting the diversity of animals observed by WSRs [7,15,19]. However, recent studies have demonstrated the ability of electromagnetic modelling software to successfully simulate the RCS of airborne animals in general [9,16]. Such analyses have the potential to bridge the information gap between weather radar observations and in situ data and enable accurate quantitative assessments of volant animals over large scales.

Alongside these technological developments, data associated with natural history collections are a fast-growing resource for scientists interested in investigating environmental change in the broad absence of long-term systematic monitoring data [20,21]. This growth is partly due to efforts to digitise these collections, making specimens stored in museum collections and their associated metadata more accessible to researchers, especially those from different disciplines [21,22]. Electromagnetic modelling software may be combined with high-definition, three-dimensional imagery collected using photogrammetry or computed tomography (CT) as part of the digitisation process to model insect RCS data more accurately. However, what is unclear in this new area of research is the level of detail required of the input specimen and to what extent different anatomical features might influence the RCS.

In this study, these tools, which are now readily accessible to radar aeroecologists, are used to explore in detail and document the considerations of modelling the RCS of a noctuid moth. As in Mirkovic et al. [9], the focus of this study is on insects, as there are a distinct set of difficulties in quantifying properties such as insect abundance, biomass, and morphotype using WSRs when compared to other volant organisms, due to their size in relation to the wavelengths of WSRs and their density within the air column. Unlike the work of Mirkovic et al. [9], which focused on examining the use of prolate spheroids and ellipsoids to model a broad range of species, this study focuses upon a single specimen, a noctuid moth, and begins with a model that is anatomically correct, as in Mirkovic et al. [16] for the Brazilian free-tailed bat (*Tadarida brasiliensis*), and works backwards towards an equivalent prolate ellipsoid model. This has enabled us to explore the implications of the various assumptions that may be made when modelling the RCS of an insect that has a body length comparable to the wavelengths of WSRs and dedicated entomological radars [7]. Through this process, the role of the specimen's morphology and composition, the two most important considerations in determining its RCS, are described. Specifically, throughout this article, we examine the following three hypotheses: (i) that high-fidelity, three-dimensional scans provide a more accurate representation of the RCS of an insect than simple ellipsoids; (ii) that the morphology of an insect impacts upon its RCS; and (iii) that the modelled composition of an insect impacts upon its RCS.

2. Materials and Methods

2.1. Overview

The most important and time-consuming step was the creation of the anatomically correct 3D specimen model. Here, a detailed model was created to start our investigation to explore the impact the level of morphological detail has on RCS values. This guided further efforts to determine the RCSs of insects where prolate ellipsoids do not provide enough fidelity [9]. Initially, the surface topology of the noctuid moth was created from data collected by a micro-CT scan of the specimen using software to retopologise the outer surface of the insect's exoskeleton with the highest fidelity possible. The scan resulted in a 3D model that could be simplified in stages to examine which morphological structures have the most impact on the insect's RCS, and be compared to basic geometric shapes, as tested in previous studies [9]. Using data from the literature, we then explore the role of different compositions and morphological combinations of composition on determining the

insect's RCS. Throughout this work, we use the RCS data compiled for noctuid moths that form part of the larger RCS dataset compiled by Drake et al. [19] as a comparison to our modelled values. As such, we limit our comparisons to the maximum (σ_{xx}; also referred to as the parallel or along-body) and the minimum (σ_{yy}; also referred to as the transverse or across-body) ventral aspect X-band (9.4 GHz) RCS values.

2.2. Description of the Specimen

The Noctuidae are the most species-rich family of moths in the UK [23], with all species sharing a similar morphotype. Noctuid moths have formed the focus of several past aeroecological studies, primarily due to their importance as migratory crop pests [24–30], in addition to UK-based research concerning nocturnal aerial insect density, dispersal, and migration [31–34]. Our focal noctuid specimen is a male *Xestia xanthographa*—a common species found throughout the UK which occupies a wide range of urban and semi-natural habitats [23,35]. The body of the *X. xanthographa* specimen is approximately 17 mm in length (measured from the anterior margin of the pronotum to the posterior margin of the final abdominal segment, not including the genitalia) and 5.1 mm in width (measured across the widest point of the thorax). The antennae are filiform and complete. The forewings are 20 mm in length. Species identity was confirmed using molecular methods (see Appendix A).

2.3. 3D Modelling

To create a 3D model of the moth, the specimen was coated with 20 nm of gold-palladium using a Cressington Sputter Coater 208HR and scanned using the Nikon Metrology HMX ST 225 micro-CT system at the United Kingdom's Natural History Museum Imaging and Analysis Centre, London.

The raw micro-CT scan (Figure 1a) was imported into the open-source software, 3D Slicer [36], to segment the pixels representing the specimen from the rest of the scan and to create a 3D mesh of the surface of the segmented volume of data (Figure 1b). 3D Slicer has an adaptive threshold function, providing upper and lower limits of intensity, that allowed us to reduce background clutter within the scan whilst preserving as much of the specimen as possible. The resultant data, representing the volume of the specimen, proved too complex to be used in WIPL-D, which requires a single surface mesh. Therefore, the Slicer model was exported to the open-source software Blender [37] as a surface mesh, in a stereolithography (STL) file format. A single surface mesh was then created by retopologising—digitally tracing over the specimen to create a new mesh—using the ReTopoFlow [38] add-on tool within Blender (see Figure 2). This mesh also incorporated any major air cavities that a noctuid would typically contain, such as large air sacs linking to the respiratory system [39,40], resulting in the internal air cavities being directly connected to the outer surface of the moth's exoskeleton within the mesh.

The hindwings were reconstructed due to a loss of detail with thresholding and deformation by the vacuum created during the sputter coating process, and were therefore digitally unfolded and repositioned, using Blender, into a more realistic mid-flight position (Figure 2); the positioning of the legs and antennae were also adjusted to reflect this. To examine the role of wing positioning on the RCS, Blender's animation tools were used to pose the specimen in different flight positions.

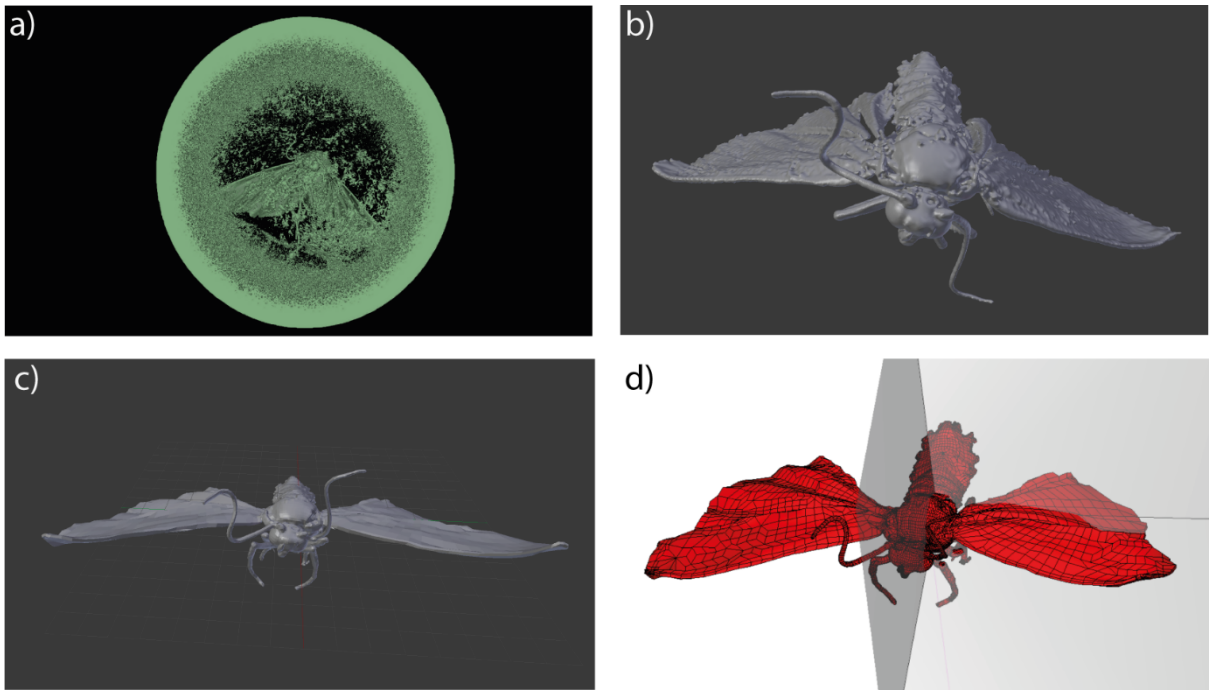

Figure 1. Illustration of the steps taken to convert the micro-CT scan data into the mesh used by WiPL-D: (**a**) depicts the micro-CT data within Slicer 3D, with limited thresholding applied; (**b**) depicts the final stereolithography data exported from Slicer 3D and used in Blender to create a 3D mesh of the specimen's surface; (**c**) shows the final 100% resolution 3D model of the specimen created in Blender; (**d**) depicts the mesh of the 3D model created in WiPL-D using only 25.0% of the number of plates of the 100% resolution model.

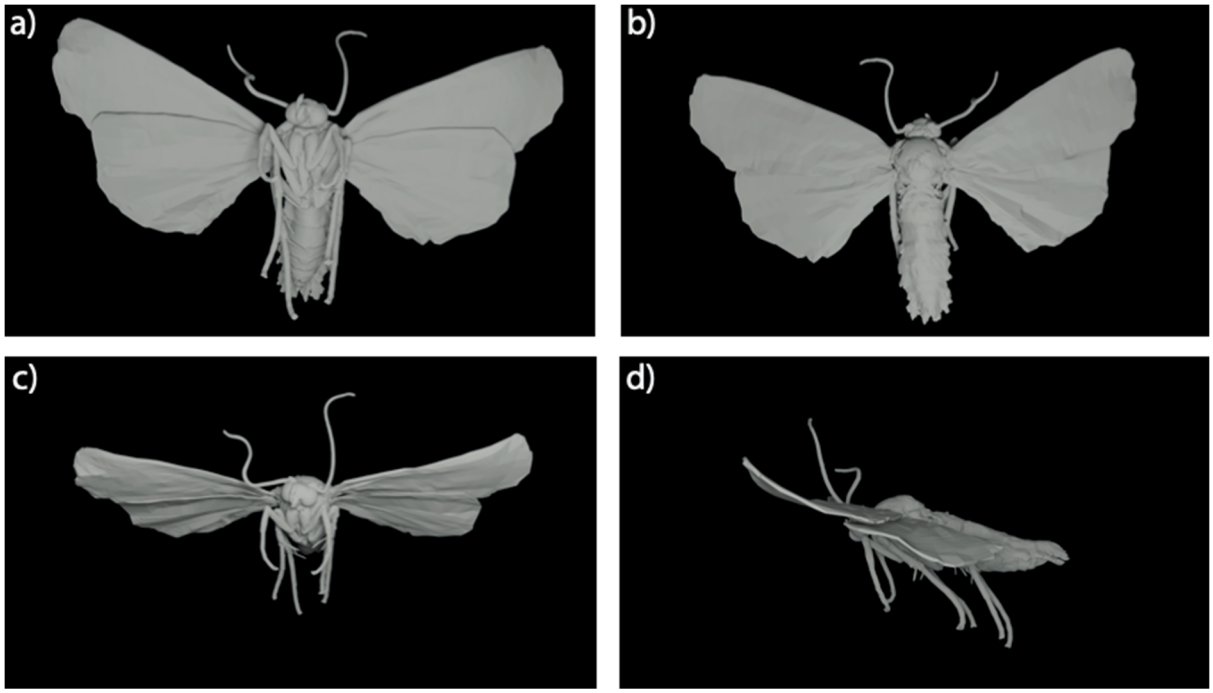

Figure 2. Depictions of the (**a**) ventral/bottom, (**b**) dorsal/top, (**c**) anterior/front, and (**d**) lateral/left-hand side views of the final 100% 3D model of the noctuid moth specimen.

2.4. Electromagnetic Simulations

As in Mirkovic et al. [9,16], we use the WiPL-D Pro 3D Electromagnetic Solver [41,42] to calculate the RCS of the specimen. WiPL-D uses a solving technique known as the Method of Moments (MoM). Within this framework, the shape of the three-dimensional object is represented by a set of interconnected plates in a quadrilateral mesh. The internal composition of the object is defined in terms of dielectric constant and loss factor, while the frequency, incident aspect angle and polarisation of the electromagnetic field may be defined by the user. Note that WiPL-D is one among several available electromagnetic modelling software packages able to simulate the RCS of an insect. The focus of this study is not to explore the accuracy of WiPL-D or any other software in particular, rather it is on the use of such software to explore the parameter space of insect RCSs.

To explore the parameter space that comprises factors that are important for accurately modelling the RCS of the specimen, we ran several sets of simulations where we changed single parameters of the model. These included (i) model resolution (i.e., the number of plates represented by the quadrilateral mesh with respect to the 100% model in Figure 2); (ii) model morphology; and (iii) model composition. Each of these sets of simulations is described below. For all simulations, WiPL-D was configured to mimic a linearly polarised vertically pointing 9.4 GHz radar so that our results could be compared to the data in Drake et al. [19] and would be applicable to the observations of other ZLC (Zenith-pointing Linear-polarised Conical scan radars) [43–45]. These simulations were conducted after extensive testing with WiPL-D to determine the optimal settings (see Appendix B) for the simulations. To conduct the simulations, the STL of the specimen was first imported into the WiPL-D Pro CAD software to convert the STL into the proprietary format utilised by WiPL-D software suite. Pending the morphological and compositional changes needed for each simulation, the model was either modified in Blender before being imported into WiPL-D or the change was made in WiPL-D itself. The interplay between these tools was crucial for creating the model configuration used below.

2.5. Model Resolution

The first set of simulations was a series of model decimations (reductions in resolution) to determine the necessary overall detail of the model needed to simulate the RCS of a noctuid moth. The aim was to find the lowest number of plates that would have an RCS that was not significantly different from that of the 100% model. This process was carried out to understand the level of detail needed to model future specimens as well as to determine the computational time needed to complete our series of simulations. Both are practical considerations that need to be accounted for to enable future RCS simulations of organisms.

To determine the lowest number of plates required, using Blender's Decimate Modifier tool, we reduced the total number of plates within the 100% model in increments of 12.5% from 87.5% to 12.5% and then we proceeded to reduce the model's complexity by halves until we had a model with less than 1% (~0.8%) of the number of plates of the original model. Figure 3 shows a representative sample of these models up to the 25.0% model of the total number of plates; visual differences are hard to distinguish between models with more plates in this 2-D representation. Note that in Blender, the 25.0% model was composed of 29,256 faces, and these were converted into 35,111 plates by WiPL-D. These 11 simulations were compared to assess the difference between model resolutions. We were unable to simulate the RCS of the 100% version of the model due to software constraints. As such, the 87.5% model was used as the standard against which the simulation results of the more highly decimated models could be compared. Figure 3 shows a sample of model decimations simulated in this study. Significant changes can easily be seen between the decimations shown.

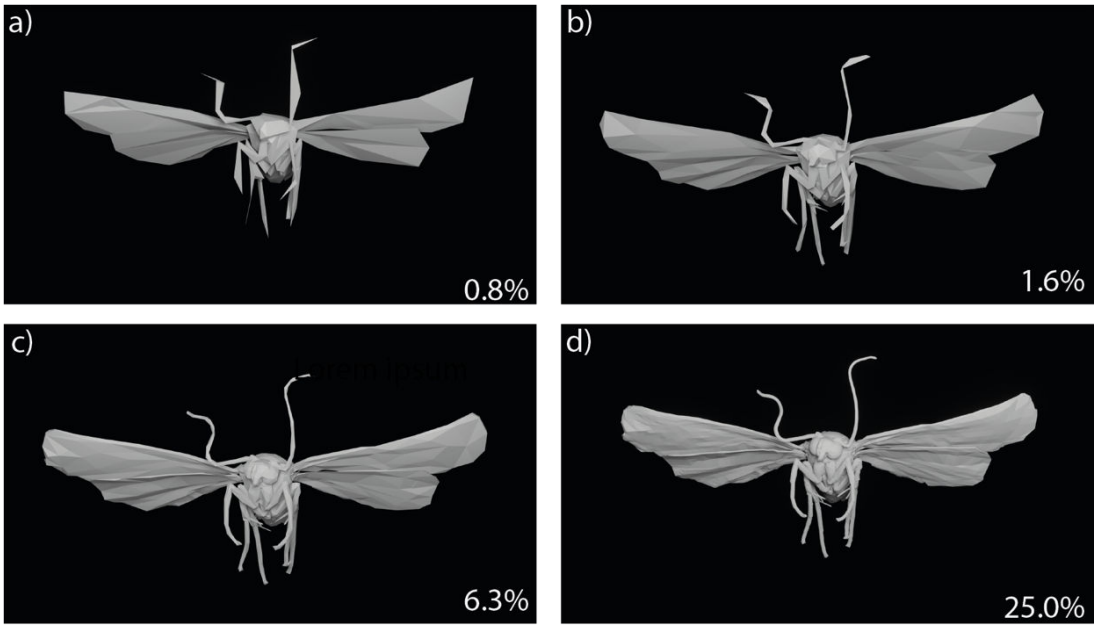

Figure 3. Depiction of four models representing the range of decimations modelled in this study: (**a**) 0.8%, (**b**) 1.6%, (**c**) 6.3% and (**d**) 25.0%. The percentage indicates the percentage of plates that comprises each model compared to the full resolution model.

2.6. Model Morphology

After exploring what complexity was necessary to model our specimen, we ran a series of simulations aimed at exploring the role of body morphology on an insect's RCS. This series and all further simulations use the model that was decimated to 25.0% of the original model. The evidence to support this decision is discussed in the results.

To assess the role of body morphology, we ran multiple simulations using: (i) the "Full" model (Figure 4a), complete with body, wings, and legs and antennae; (ii) the "Wingless" model (Figure 4b), without wings but inclusive of the legs and antennae; and (iii) the "Body Only" model (Figure 4c), without wings or legs and antennae. We also conducted simulations of the Full model in three different flight wing positions (see Figure 5). The removal and repositioning of different anatomical structures allowed for their contribution to the overall RCS to be assessed. In addition to the external morphology, the contribution of internal air sacs and the genital "cavity" were also examined. This allowed us to assess whether such detail is necessary to capture when scanning the specimen for the purpose of exploring a specimen's RCS.

In addition to questions concerning the impact of specific structures on the specimen, we also explored how the overall size of the specimen impacted the resulting RCS. This was done by scaling the entire model in gradations of 12.5% from 75.0% to 150% of the model's original size. This scaling spans the size range of the noctuid specimens contained in the Drake et al. [19] dataset. As noctuids increase in size, certain parts of the body, including the wings, legs, and antennae do not necessarily scale linearly in terms of their thickness. Changes in body width and depth (measured here at the widest/deepest point of the thorax) are also probably greater in these simulations than they would be in reality, as we could only apply scaling uniformly to the whole moth. Therefore, these model gradations may not necessarily provide biologically realistic representations of a noctuid at each of these scales but should provide an indication of how RCS changes with scale.

2.7. Model Composition

The dielectric constant and loss factor (i.e., the permittivity) is a significant source of uncertainty in the RCS parameter space of insects. These values will vary depending on the overall composition and internal temperature of the insect, as well as the frequency being used to observe the insect [46]. Previous studies have explored relatively few dielectric constants [9,16] and used values for these materials that are representative of temperatures (~10–15 °C) well below the known internal flight temperatures of insects (~20–40 °C), specifically moths [47–49]. Here, we examine this parameter space further using data primarily from Nelson et al. [46] to describe the internal composition of the specimen, as well as values from Chen et al. [50] to describe the antenna, legs, and wings. The dielectric constant and loss factors used in this study are described in Table 1.

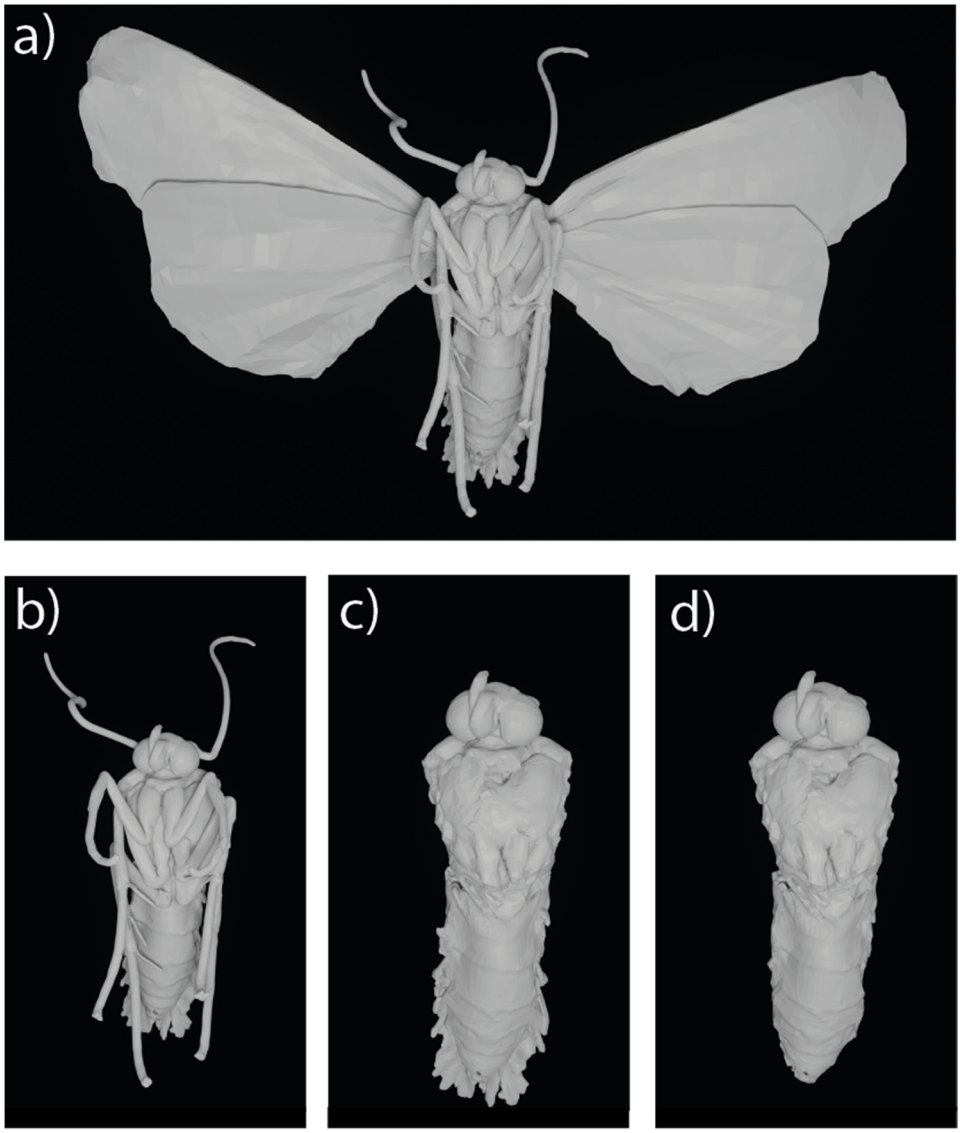

Figure 4. The ventral view of the 4 specimen morphologies examined in this study: (**a**) the Full model, depicts the complete morphology of the moth, while (**b**) the Wingless model excludes the wings, (**c**) the Body Only model further excludes the legs and antennae, and (**d**) depicts the Body Only model and further excludes the hair covering the thorax and the abdomen.

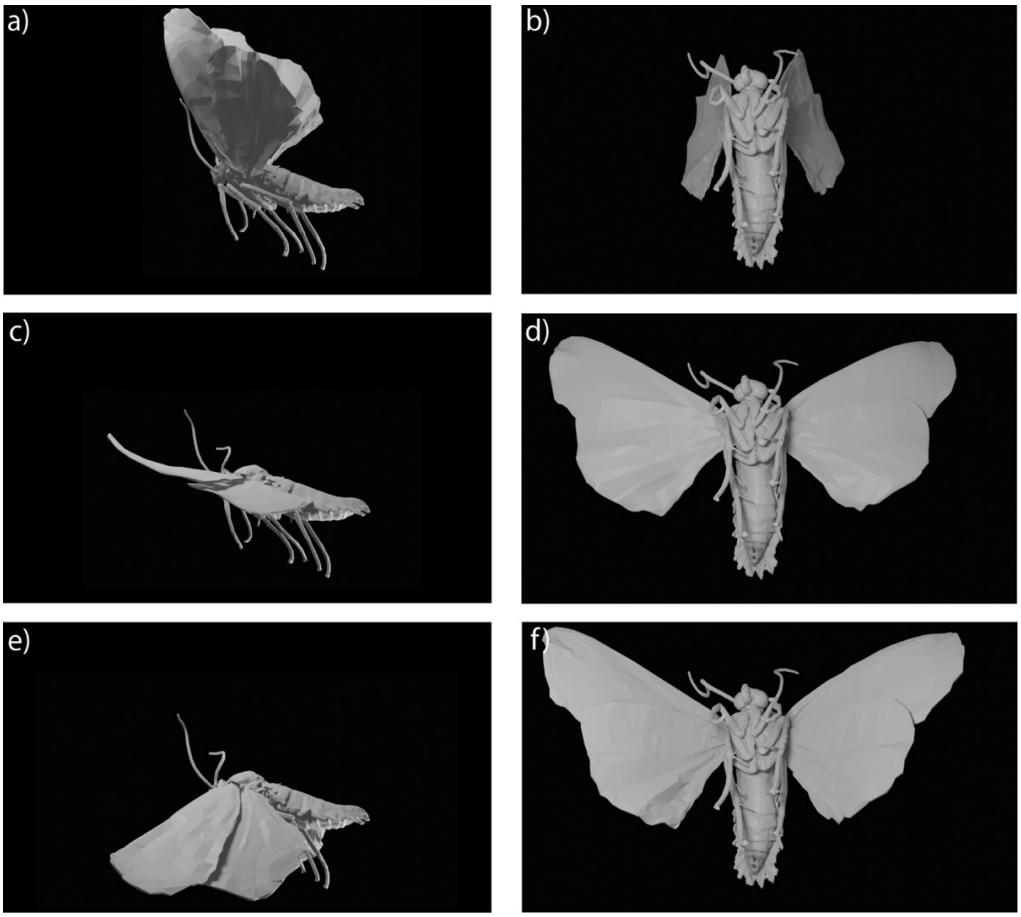

Figure 5. The three wing positions simulated as part of this study: (**a**,**b**) are referred to as "Up", (**c**,**d**) are referred to as "Mid" and (**e**,**f**) are referred to as "Down"; (**a**,**c**,**e**) depict the left-hand lateral view along the anteroposterior aspect of the moth, whilst (**b**,**d**,**f**) depict the ventral aspect.

Table 1. Dielectric constant and loss factors used in this study. All parameters are valid for 9.4 GHz.

Material	Description	Dielectric Constant	Loss Factor	Abbrev.	Density (g/cm^3)	Source	Notes
Homogenised blend of the lesser grain borer beetle	Insect paste utilised by Mirkovic et al. [9] for the lesser grain boorer, *Rhyzopertha dominica*. Temperature unspecified.	34.3	−18.6	MirkLGB	1.26	[9,46]	Used to compare the simulations of this study to Mirkovic et al. [9]. Values are taken directly from Nelson et al. [46] as part of the four species examined therein.
Homogenised blend of the rice weevil	Insect paste of the rice weevil, *Sitophilus oryzae*, at 25 °C.	30.6	−16	NelsonRW25	1.29	[46]	
Homogenised blend of the red flour beetle	Insect paste of the red flour beetle, *Tribolium castaneum*, at 25 °C.	34.0	−19.4	NelsonRFB25	1.29	[46]	

Table 1. *Cont.*

Material	Description	Dielectric Constant	Loss Factor	Abbrev.	Density (g/cm^3)	Source	Notes
Homogenised blend of the saw-toothed grain beetle	Insect paste of the sawtoothed grain beetle, *Oryzaephilus surinamensis*, at 25 °C.	39.8	−20.8	NelsonSGB25	1.34	[46]	
Chitin	Chitin film at room temperature.	4.1	−0.16	ChenMean		[50]	Extrapolated to 9.4 GHz. Values are the mean of this estimation.
Chitin	Chitin film at room temperature.	4.5	−0.18	ChenMax		[50]	Extrapolated to 9.4 GHz. Values are the maximum of this estimation.
Chitin	Chitin film at room temperature.	3.8	−0.14	ChenMin		[50]	Extrapolated to 9.4 GHz. Values are the minimum of this estimation.
Water	Water used in Mirkovic et al. [9]. Temperature unspecified.	60.3	−33.1	MirkWater	1.00	[9]	Used to compare the simulations of this study to Mirkovic et al. [9].

To examine the impact of dielectric constant and loss factor, we ran a series of simulations of different dielectric properties. For our simulations to be more representative of a live insect body, which is composed of different materials, i.e., chitin, hemolymph, viscera, etc., we divided the insect into two sections: the abdomen, thorax and head were treated as the body, while the wings, legs, and antennae were treated as appendages. The dielectric constant of the insect body was systematically changed using the materials listed in Table 1, so that the differences between the specified parameters could be directly compared. The range of values tested was chosen to represent the range of measured values found in the literature [7]. ChenMean (Table 1) was selected as a representative dielectric constant for the appendages for all the simulations.

2.8. RCS Reference Dataset

As we were unable to directly measure the RCS of the specimen modelled here (as is the case with most insects observed with radars), we compare our results to a range of RCS measurements from specimens with a similar morphology. The goal of this comparison is to help understand if the model and any perturbations we make are within the bounds of what is observed in nature rather than to try and recreate the RCS of a particular specimen. Mirkovic et al. [9] used the full Drake et al. [19] dataset in a similar manner to compare their ellipsoidal models to measured values.

Drake et al. [19] compiles and describes ventral aspect RCS values and polarisation patterns at X-band frequencies (~9.4 GHz) from 4 sources. The complete dataset, which is split into 2 parts, includes data points for 235 specimens comprising 65 species. Notably, the data also include information on mass, body length, body width and wing length for most specimens. For a full description of the dataset, please see Drake et al. [19]. From this dataset, we extracted all the information about noctuid moths. This comprised 78 individual entries from the dataset. Figure 6 depicts the variation in several morphometric traits extracted from Drake et al. [19] for the purposes of this study.

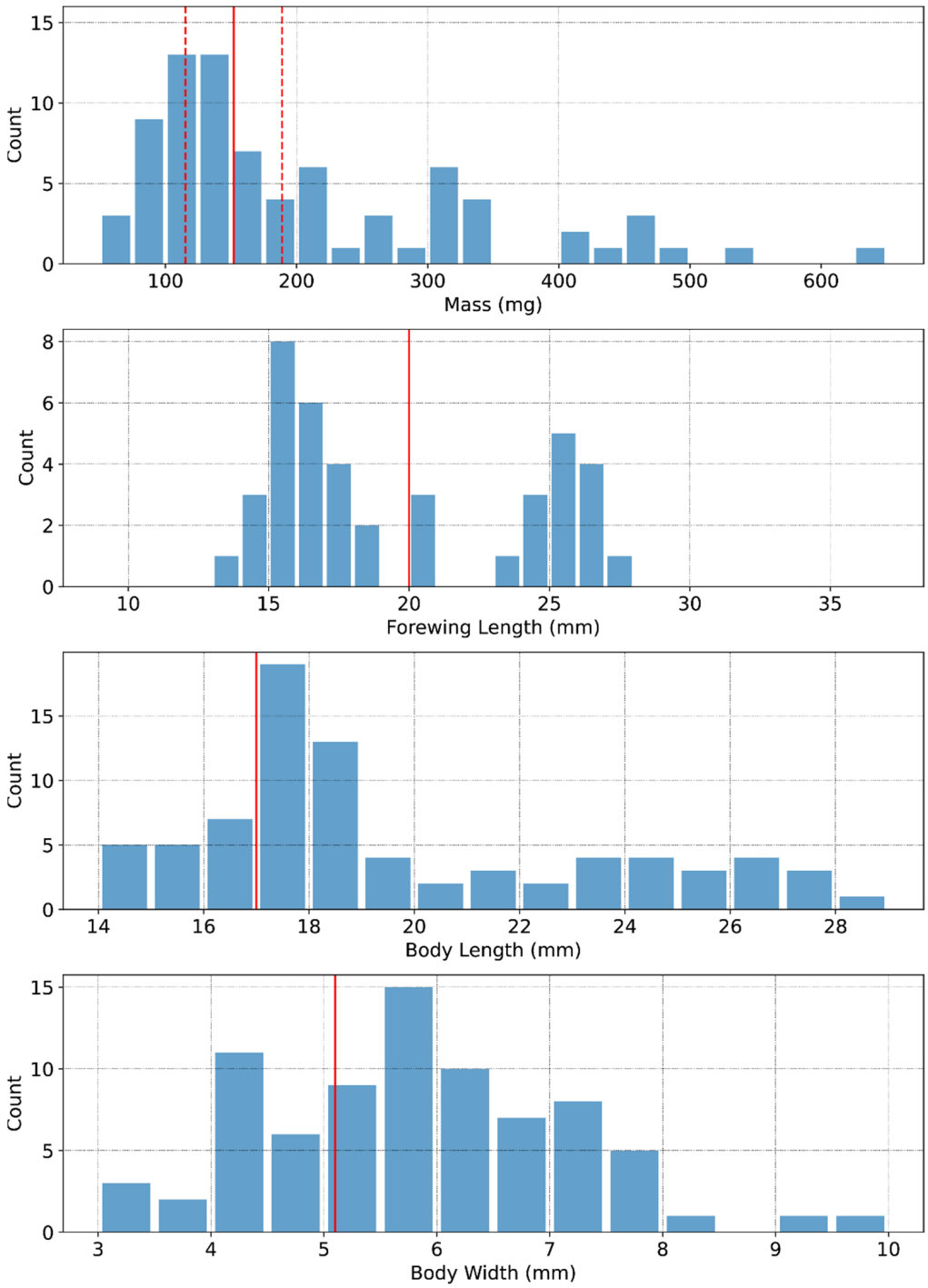

Figure 6. Distribution of morphological attributes of the noctuid specimens in the Drake et al. [19] compared to the specimen (red vertical line) modelled in this study. For the mass of our specimen, we also include the 95% confidence interval of the estimation as the dashed lines.

3. Results

The results are separated into sections that focus on different sets of simulations conducted within this study. The results also build upon each other, where the results in earlier sections inform the modelling used in later sections.

3.1. Model Resolution versus RCS

Here, we show the results of the model simulations at different levels of model decimation (number of plates). Figure 7 compares the modelled polarimetric RCS values of the 4 model decimations shown in Figure 3 compared to the highest-resolution model that we were able to simulate (87.5%). Large differences at the maximum RCS values (i.e., at 0° and 180°, or when the incident polarization is aligned along the body of the specimen) for models with <6.3% of the initial number of plates are evident, and differences at all angles exist. To examine this more closely, the σ_{xx}, σ_{yy} and their ratio for each level of decimation is shown in Figures 8 and 9.

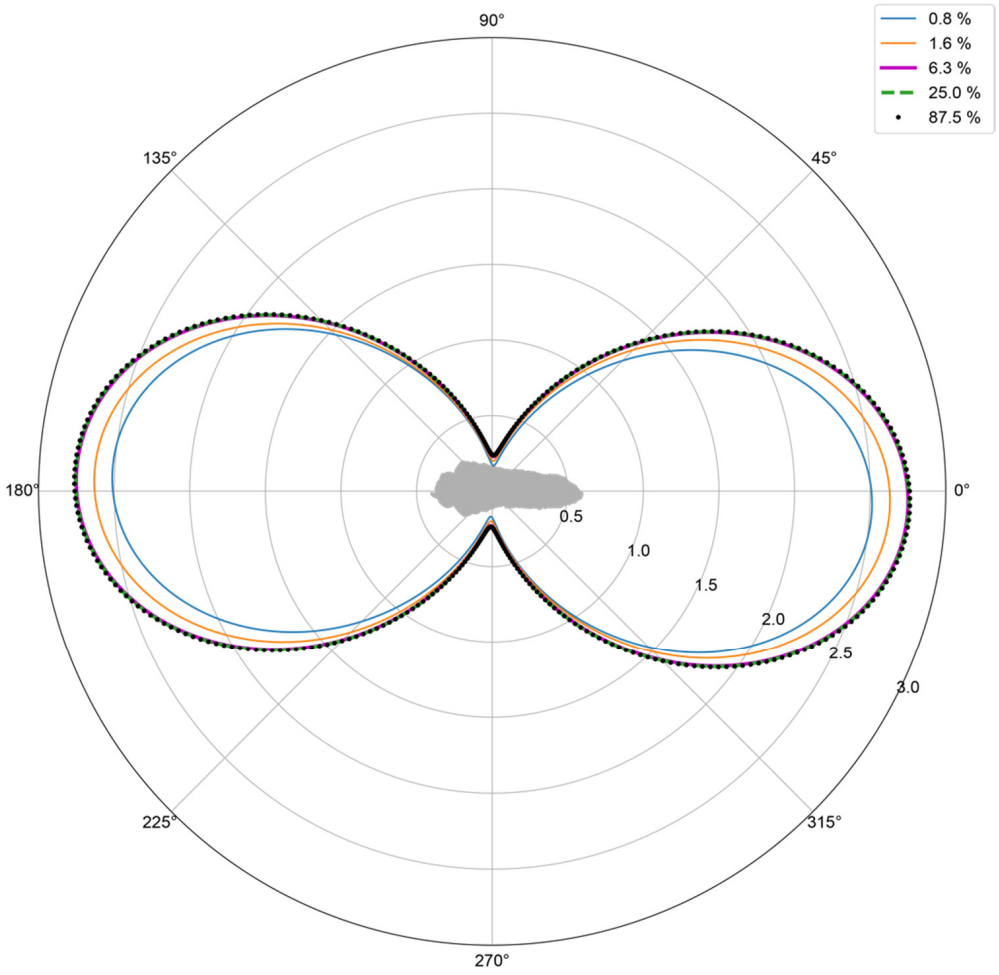

Figure 7. Comparison of the modelled polarimetric RCSs (cm^2) shown for the range of model decimations shown in Figure 3 with the addition of the highest fidelity model that we could achieve at 87.5%. These values are based on an incident radiation of 9.4 GHz at a ventral incident angle and use the simulation that excludes the impact of the wings and the legs and antennae, using the Body Only model and assumes a dielectric constant equal to that of MirkLBG (Table 1). The shadowed model is not to scale and for orientation purposes only.

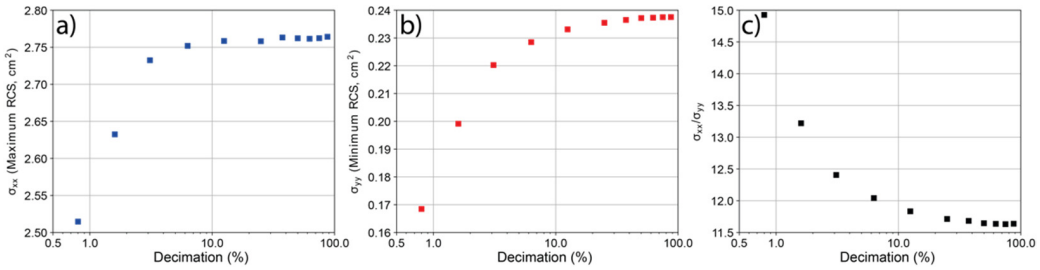

Figure 8. (**a**) Modelled maximum (σ_{xx}) and (**b**) minimum (σ_{yy}) RCS values, and (**c**) their ratio (σ_{xx}/σ_{yy}), for all decimations simulated in this study. These values are based on incident radiation of 9.4 GHz at a ventral incident angle and are from a simulation that excludes the impact of the wings, legs and antennae and assumes the specimens has a dielectric constant equal to that of MirkLBG (Table 1).

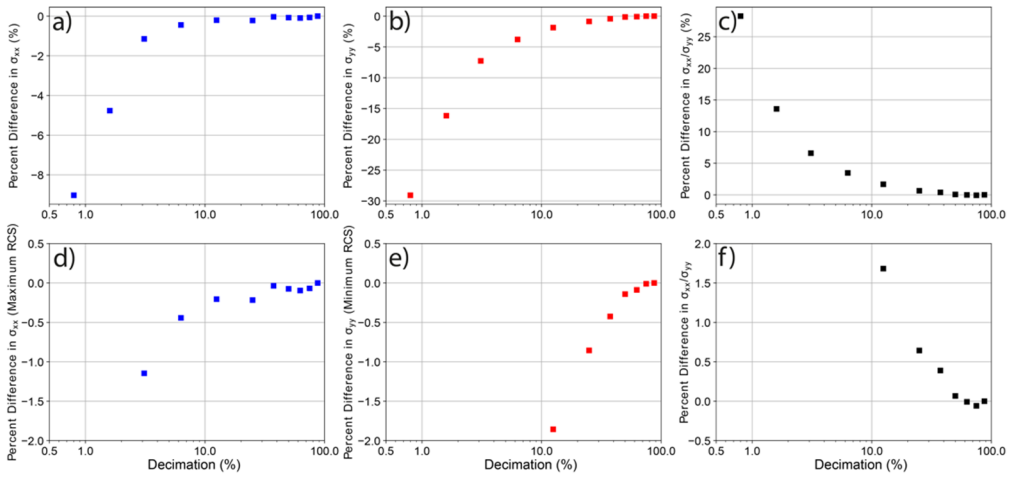

Figure 9. Percentage difference in the modelled (**a**,**d**) maximum (σ_{xx}) and (**b**,**e**) minimum (σ_{yy}) RCS values, and (**c**,**f**) their ratio (σ_{xx}/σ_{yy}), for all decimations compared to the 87.5% model. The top row shows this full range of values while the bottom row zooms in to show only differences of less than 2%.

Figure 8 shows a marked change in RCS values as the number of plates increases from approximately 1% to 10% of the highest-resolution model. From this point onward, as the complexity of the model increases the change in RCS values begins to converge. To quantify these differences, the percentage difference between each RCS value compared to 87.5% is shown in Figure 7. For all 3 metrics, we show differences of less than 1% for models that have ~25.0% the number of plates of the original model.

In addition to the fidelity of the results, another important consideration for determining the ideal model complexity is the amount of time required to run the simulation—as multiple simulations are needed. This will depend on local computing resources (see Appendix C); but in the simulations conducted here, the 0.8% simulation had a run time of ~4.5 min while the simulation of the 87.5% model took 39.6 h. For the 25.0% model, the simulation took ~5 h.

3.2. Model Morphology

Here, we show the results of a series of simulations that explore the role of model morphology and composition in the resulting RCS of the specimen. Previous work has focused on the use of prolate spheroids and ellipsoids to model the morphology of insects [9]. In Figure 10, we compare the ventral RCS of a prolate ellipsoid to a simulation of the specimen that only contains its body (the Body Only model), as well as a model including the wings, legs, and antennae (the Full model). The prolate ellipsoid was constructed following the

method in Mirkovic et al. [9] in which the length, width and mass of our specimen were used to define the dimensions of an ellipsoid of equal mass, length, and width. Figure 10 shows that prolate ellipsoid simplification overestimates the RCS of the specimen but does capture the polarimetric pattern. Figure 10 also shows that the inclusion of wings, legs and antennae modifies both the along-body and cross-body RCS values.

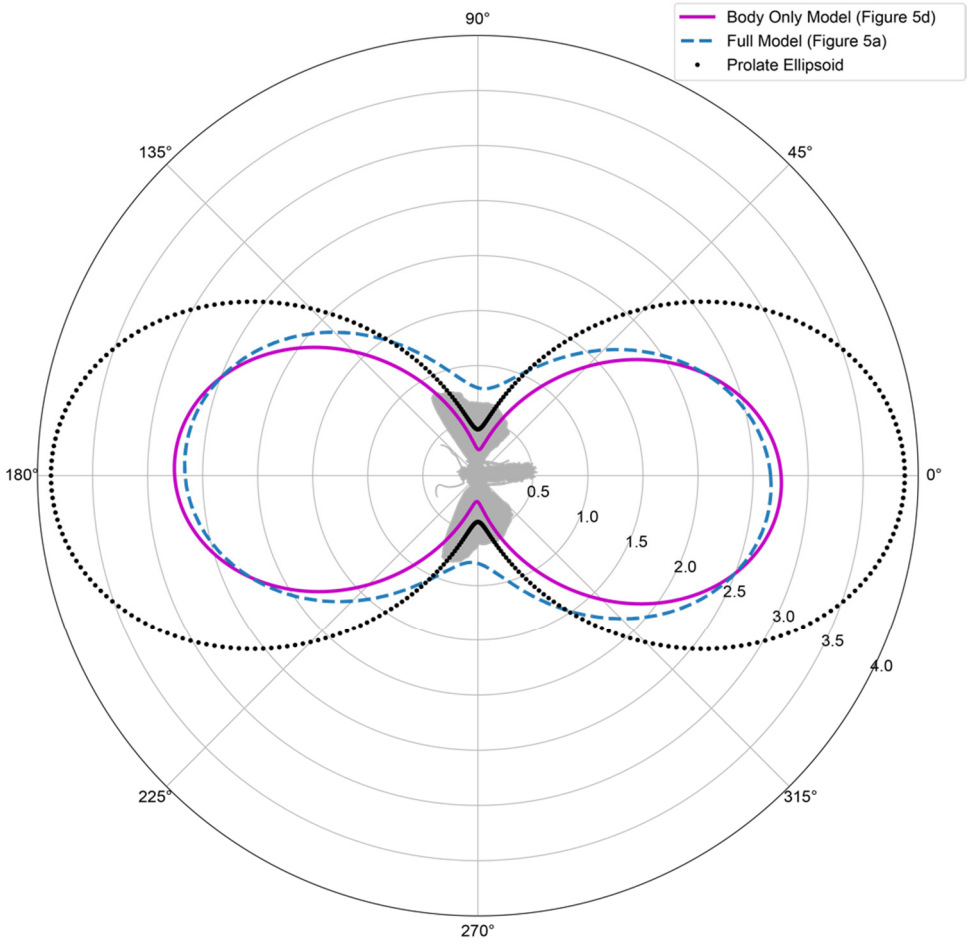

Figure 10. Comparison of the modelled polarimetric RCSs (cm^2) for the Body Only model (Figure 4d), the Full model (Figure 4a), and a prolate ellipsoid whose parameters where derived using Mirkovic et al. [9]. All models are based on the 25.0% decimation model in Figure 7 and use dielectric constant and density equal to that of MirkLBG. The Full model uses ChenMean as the dielectric constant for the wings, and legs and antennae (Table 1). The shadowed model is not to scale and for orientation purposes only.

Related to morphology is the positioning of the specimen's wings. In Figure 11, we show the results of simulations of the specimen as depicted in the three flight positions shown in Figure 5. There is a clear difference in RCS magnitude for each of the positions. This, along with differences shown in Figure 10 between the Body Only simulation and the simulation of the Full model, show that the inclusion of the wings and their position significantly impacts the RCS of the specimen.

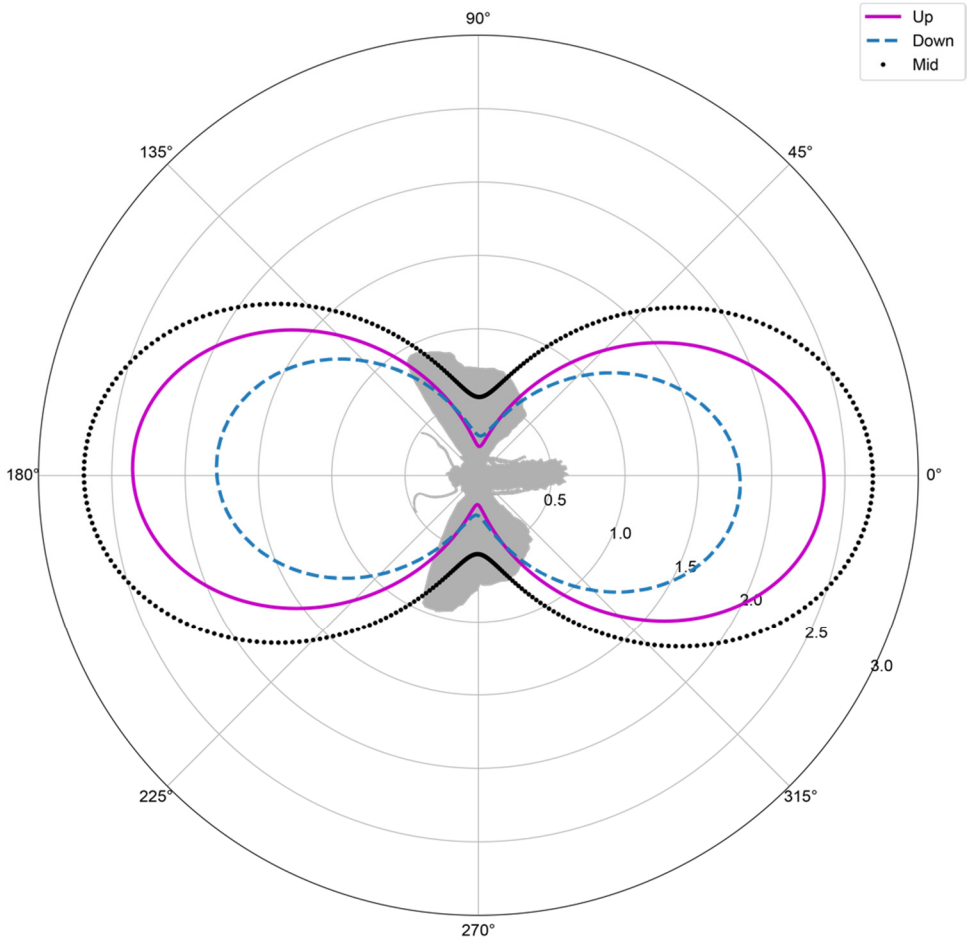

Figure 11. Comparison of the modelled polarimetric RCSs (cm^2) showing the results for a model with the three different wing positions: Up, Mid and Down shown in Figure 5. The shadowed model is not to scale and for orientation purposes only.

3.3. Composition

To isolate the role of model composition, in Figure 12, we compare a series of simulations of the Body Only model (Figure 4c) where the internal dielectric constant of the body was varied using the values listed in Table 1. Filling the whole specimen with the same dielectric constant is not realistic from a physiological perspective, hence in Figure 12 we solely use the Body Only model. However, we tested the full diversity of internal compositions, from those used in previous models (e.g., water and MirkLBG) to the inclusion of chitin, to illustrate the impact of these choices on RCS values. The along-body (σ_{xx}) results fall into two clusters: (1) simulations that used dielectric constants derived primarily from chitin-only based materials, which generally have a much smaller RCS (~0.25 cm^2); and (2) simulations with dielectric constants derived from measurements of insect paste (which contains water along with chitin and other organic matter), which have a higher RCS (~2.8 cm^2). These differences are much less pronounced for cross-body (σ_{yy}) RCS values, but the relationship is similar. Interestingly, the results for σ_{yy} show that assuming that the specimen is composed only of water (MirkWater) causes an overestimate of the RCS value. The ratio of along-body to cross-body (σ_{xx}/σ_{yy}) shows the separation of the various compositions examined here and shows a better match between dielectric constants derived from insects with the measured values from Drake et al. [19].

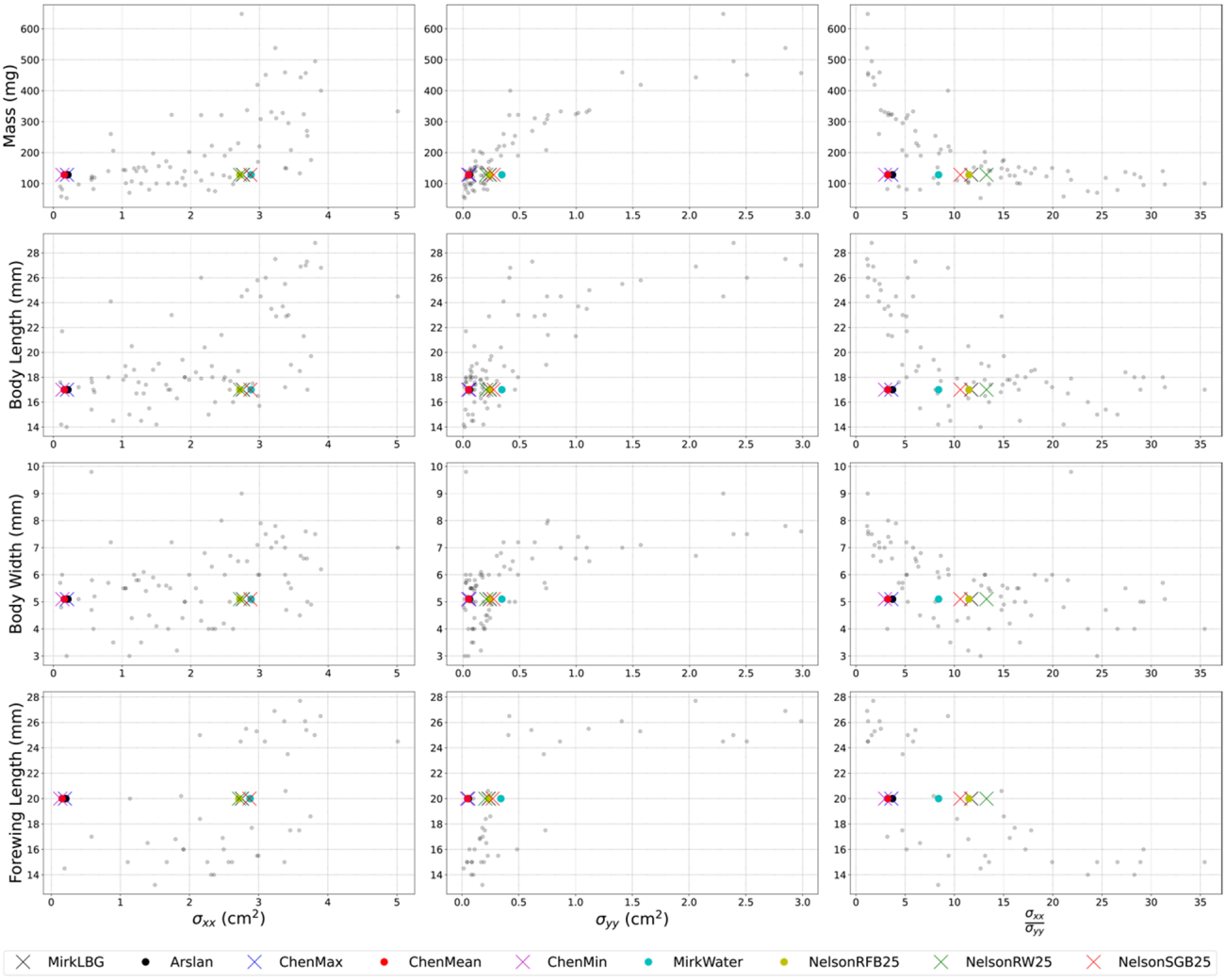

Figure 12. Comparison of a series of simulations of the Body Only model (Figure 4d) where the only change was the internal dielectric constant. The grey data points represent the along-body (σ_{xx}) and cross-body (σ_{yy}) RCS values and their ratio (σ_{xx}/σ_{yy}) versus the corresponding morphological attributes reported by Drake et al. [19] for noctuid moths.

To compare the combined role of morphology and composition, Figure 13 compares the results of two simulations in which the only difference is the addition of anatomically correct appendages consistently modelled with a dielectric constant that is representative of chitin. Specifically, the bodies of both anatomical models in Figure 13 use MirkLBG as their dielectric constant, whilst the Full model also includes the wings and the legs and antennae that use ChenMean as their dielectric constant. Altering model composition by morphology and separating the three main body segments—body, wings, and the legs and antennae—creates a model that is closer to a realistic insect. This, in turn, significantly impacts the RCS of the specimen, as both the magnitude and polarimetric pattern of the RCS differ between the two simulations. Notably, the ratio of the along-body to cross-body RCS is smaller in the Full model.

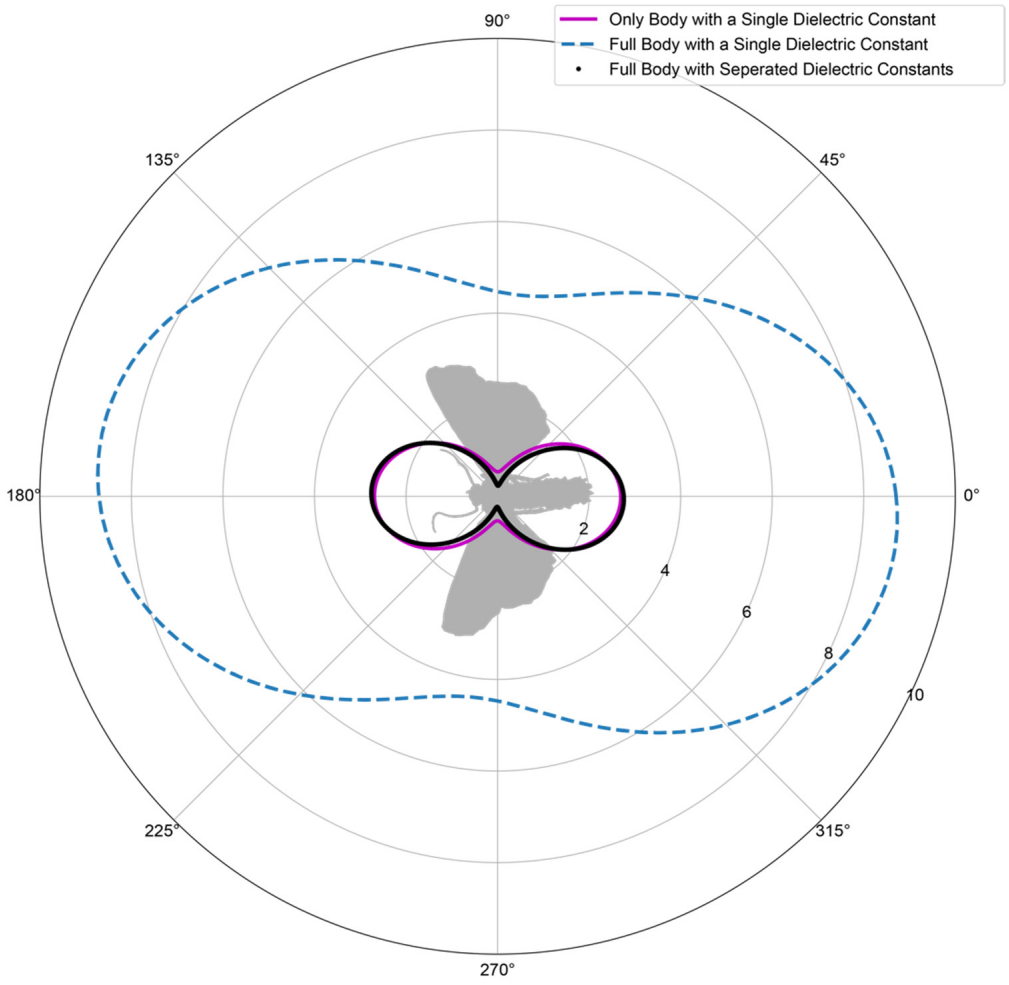

Figure 13. Comparison of the modelled polarimetric RCSs (cm^2) showing the combined differences between morphology (Full and Body Only models), and composition with the body, wings, and legs and antennae having individual or identical material/dielectric constants. The shadowed model is not to scale and for orientation purposes only.

3.4. Scaling

In addition to the sensitivity tests examining the composition of the specimen's body, we also examined the role of the overall size of the specimen. The model used for scaling consisted of the Full body model with the MirkLBG dielectric constant used for the body and ChenMean for the wings and appendages (see Table 1).

As shown in Figure 14, the along-body (σ_{xx}) results compare well with the measurements reported by Drake et al. [19]. Due to the simplified nature of our scaling, the cross-body (σ_{yy}) and the ratio of along-body to cross-body (σ_{xx}/σ_{yy}) results do not match well with these past reported measurements. Even so, the functional form of the trends of these results is similar. This suggests that if a more biologically accurate attempt at allometric scaling was made then the simulations would more quantitatively match with the measurements of Drake et al. [19].

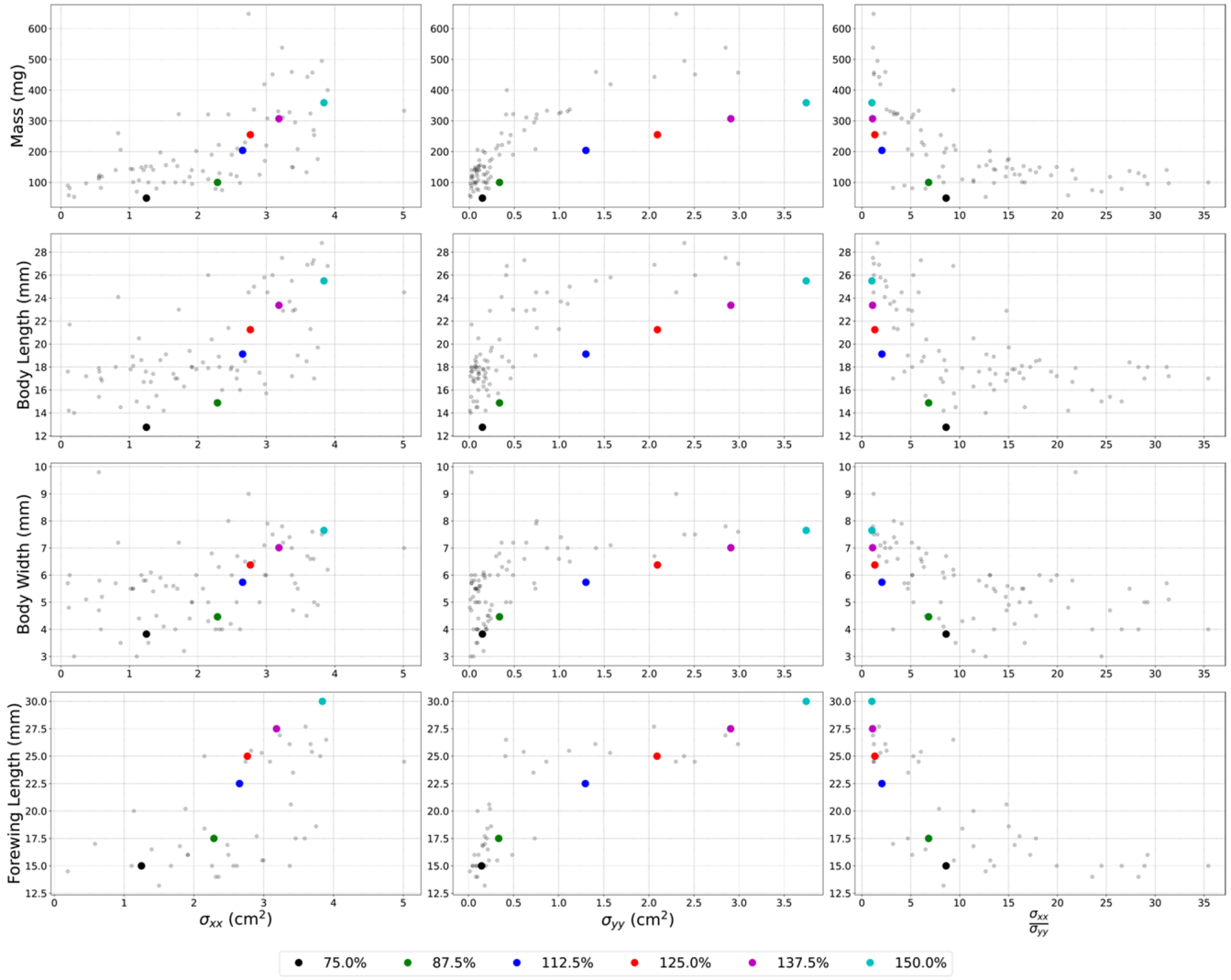

Figure 14. Comparison of a series of simulations in which the Full model (Figure 4a) has been scaled in all dimensions by the percentage indicated in the legend. The grey data points represent the along-body (σ_{xx}) and cross-body (σ_{yy}) RCS values and their ratio (σ_{xx}/σ_{yy}) versus the corresponding morphological attributes reported by Drake et al. [19] for noctuid moths.

4. Discussion

Overall, we have demonstrated a viable method of simulating the RCS of an anatomically correct noctuid moth. This study builds upon the methodology initially explored by Mirkovic et al. [9] that only examined prolate ellipsoids. Our results show that having an anatomically correct model is more representative than a general prolate ellipsoid (Figure 10), even at lower resolutions.

In addition to representing the morphology of the model accurately, we show that using the properties of a biologically accurate material as the basis for the dielectric constant of the model's body is important in simulating the RCS. Neither simulation composed of pure water or chitin compared well with the past measurements as reported by Drake et al. [19]. We note that further measurements using the techniques described in Nelson et al. [46] and Chen et al. [50] are needed to explore this underestimated space further.

We found that wings and wing positioning impacted the RCS and, thus, are important to model accurately. Note that moth fore- and hindwings are covered in a layer of scales, which may alter the relative thickness of the wings and make them less representative of the wings of the broader aerial insect community, i.e., dipteran, coleopteran, hemipteran, or

hymenopteran species [51]. In addition, the amount of time spent at a particular position is not consistent across the three flight poses, and varies between insect taxa [52,53], which is something to consider for future modelling.

We note that temperature is also a significant factor driving the value of both the dielectric constant of the insect and the loss factor of water (a major component of the insect paste in Table 1). As the internal temperature of the insect changes, this will alter the dielectric constant; however, internal temperature is not consistent throughout an insect's body. For instance, the internal temperature of a moth's abdomen can be as much as 10 °C cooler than the internal temperature of the thorax [47–49]. This is not something that we have explored here, but data are available from the wider literature [47,54] that would make such an initial study possible using similar methods to those presented here.

Combined, our investigations suggest that for modelling the RCS of a noctuid moth, the best results are achieved using an accurately scaled model that represents the body, wings, and legs and antenna in a realistic flight pose, and where the composition of the model sections are consistent with biology. The method shown here, as adapted from Mirkovic et al. [9,16], is readily applicable to other similar insect specimens. Future work should include new measurements of the RCS of insects, such as those made by Kong et al. [55]. Additionally, simulations of aerial aggregations of insects with varying densities of individuals and body configurations (i.e., wing-beat phase) should be explored to understand how the RCS of a single insect scales. These explorations will be essential to quantitatively interpreting the results of WSRs and special-purpose entomological radars.

Author Contributions: R.R.N.III, C.H. and E.J.D. conceived the research and acquired the funding; F.I.A. undertook 3D and RCS modelling; T.D. and E.J.D. advised on some of the anatomical decisions for the creation of the model; T.D., W.L.E. and E.J.D. collated moth traits data; E.J.D. and J.R. carried out molecular identification of the moth specimen; all authors contributed to the writing of this paper. All authors have read and agreed to the published version of the manuscript.

Funding: This research was funded by a Natural Environment Research Council (NERC) Standard Grant (NE/S001298/1).

Institutional Review Board Statement: Not applicable.

Informed Consent Statement: Not applicable.

Data Availability Statement: All simulation data and 3D models used in this manuscript are available upon request from the authors.

Acknowledgments: We would like to thank the Natural History Museum, London, for providing access to their micro-CT scanning facilities, and Vincent Fernandez and Brett Clark from the NHM's Imaging and Analysis Centre for their time and expertise. We also wish to thank Charles Fletcher and Roger Key for providing us with moth specimens, and Milos Pavlovic at WiPL-D for his support in learning and diagnosing the software.

Conflicts of Interest: The authors declare no conflict of interest. The funders had no role in the design of the study; in the collection, analyses, or interpretation of data; in the writing of the manuscript, or in the decision to publish the results.

Appendix A. Molecular Identification of *X. xanthographa*

DNA was extracted from one moth leg using the HotShot method, a modified alkaline lysis protocol [56]. A region of the cytochrome c oxidase mitochondrial gene was amplified from extracted DNA using two primer sets; HCO2198 (TAA ACT TCA GGG TGA CCA AAA AAT CA) and LCO1490 (GGT CAA CAA ATC ATA AAG ATA TTG G) [57] and LepF (ATT CAA CCA ATC ATA AAG ATA TTG G) and Lep R (TAA ACT TCT GGA TGT CCA AAA AAT CA) [58]. HCO2198/LCO1490 PCR product (709 bp) were cloned into the pEASY—T3 Vector (TransGen Biotech) and the LepF/LepR PCR product (658 bp) was purified using the Monarch PCR purification kit (New England Biolabs). PCR products and plasmids were sanger sequenced by Eurofins Genomics. Sequences were quality checked and there was 100% concordance between sequences. The moth species was then identified

using the BOLD database (http://www.boldsystems.org, accessed on 6 October 2020) as *Xestia xanthographa* with 100% probability.

Appendix B. Wipl-D Configuration Utilised in All Simulations

1. Di3 Files: Off,
2. Integral Advanced: Enhanced 1,
3. Precision: Double, and
4. OM: Monostatic.

Appendix C. Specification of the Computer Resources Used in This Study

We utilised a desktop PC with a NVIDIA GeForce RTX 2080 Ti graphics card, an Intel i9 9900X Extreme CPU, 128 GB of 3000 MHz memory and a 1TB Samsung NVMe SSD hard drive.

References

1. Crawford, A.B. Radar Reflections in the Lower Atmosphere. In *Proceedings of the IRE*; Institute of Radio Engineers IRE: New York, NY, USA, 1949; Volume 37.
2. Gauthreaux, S.; Belser, C.G. Displays of Bird Movements on the WSR-88D: Patterns and Quantification. *Weather Forecast.* **1998**, *13*, 453–464. [CrossRef]
3. Gauthreaux, S.A.; Livingston, J.W.; Belser, C.G. Detection and discrimination of fauna in the aerosphere using Doppler weather surveillance radar. *Integr. Comp. Biol.* **2007**, *48*, 12–23. [CrossRef] [PubMed]
4. Dokter, A.M.; Liechti, F.; Stark, H.; Delobbe, L.; Tabary, P.; Holleman, I. Bird migration flight altitudes studied by a network of operational weather radars. *J. R. Soc. Interface* **2011**, *8*, 30–43. [CrossRef] [PubMed]
5. Chilson, P.B.; Bridge, E.; Frick, W.F.; Chapman, J.; Kelly, J. Radar aeroecology: Exploring the movements of aerial fauna through radio-wave remote sensing. *Biol. Lett.* **2012**, *8*, 698–701. [CrossRef] [PubMed]
6. Chilson, P.B.; Frick, W.F.; Kelly, J.F.; Howard, K.W.; Larkin, R.P.; Diehl, R.H.; Westbrook, J.K.; Kelly, T.A.; Kunz, T.H. Partly Cloudy with a Chance of Migration: Weather, Radars, and Aeroecology. *Bull. Am. Meteorol. Soc.* **2012**, *93*, 669–686. [CrossRef]
7. Drake, A.; Reynolds, D.R. *Radar Entomology: Observing Insect Flight and Migration*; CABI: Wallingford, UK, 2012. Available online: https://www.cabi.org/bookshop/book/9781845935566 (accessed on 3 October 2020).
8. Stepanian, P.M.; Horton, K.G.; Melnikov, V.M.; Zrnić, D.S.; Gauthreaux, S.A., Jr. Dual-polarization radar products for biological applications. *Ecosphere* **2016**, *7*, e01539. [CrossRef]
9. Mirkovic, D.; Stepanian, P.M.; Wainwright, C.E.; Reynolds, D.R.; Menz, M.H.M. Characterizing animal anatomy and internal composition for electromagnetic modelling in radar entomology. *Remote Sens. Ecol. Conserv.* **2019**, *5*, 169–179. [CrossRef]
10. Stepanian, P.M.; Entrekin, S.A.; Wainwright, C.E.; Mirkovic, D.; Tank, J.L.; Kelly, J.F. Declines in an abundant aquatic insect, the burrowing mayfly, across major North American waterways. *Proc. Natl. Acad. Sci. USA* **2020**, *117*, 2987–2992. [CrossRef]
11. Bauer, S.; Chapman, J.W.; Reynolds, D.R.; Alves, J.; Dokter, A.M.; Menz, M.; Sapir, N.; Ciach, M.; Pettersson, L.B.; Kelly, J.F.; et al. From Agricultural Benefits to Aviation Safety: Realizing the Potential of Continent-Wide Radar Networks. *BioScience* **2017**, *67*, 912–918. [CrossRef]
12. Bauer, S.; Shamoun-Baranes, J.; Nilsson, C.; Farnsworth, A.; Kelly, J.F.; Reynolds, D.R.; Dokter, A.M.; Krauel, J.F.; Petterson, L.B.; Horton, K.G.; et al. The grand challenges of migration ecology that radar aeroecology can help answer. *Ecography* **2019**, *42*, 861–875. [CrossRef]
13. Shamoun-Baranes, J.; Nilsson, C.; Bauer, S.; Chapman, J. Taking radar aeroecology into the 21st century. *Ecography* **2019**, *42*, 847–851. [CrossRef]
14. Shamoun-Baranes, J.; Alves, J.; Bauer, S.; Dokter, A.M.; Hüppop, O.; Koistinen, J.; Leijnse, H.; Liechti, F.; Van Gasteren, H.; Chapman, J.W. Continental-scale radar monitoring of the aerial movements of animals. *Mov. Ecol.* **2014**, *2*, 9. [CrossRef]
15. Melnikov, V.M.; Istok, M.J.; Westbrook, J.K. Asymmetric Radar Echo Patterns from Insects. *J. Atmos. Ocean. Technol.* **2015**, *32*, 659–674. [CrossRef]
16. Mirkovic, D.; Stepanian, P.M.; Kelly, J.F.; Chilson, P.B. Electromagnetic Model Reliably Predicts Radar Scattering Characteristics of Airborne Organisms. *Sci. Rep.* **2016**, *6*, 35637. [CrossRef] [PubMed]
17. Knott, E.F.; Shaeffer, J.F.; Tuley, M.T. *Radar Cross Section*, 2nd ed.; SciTech Publishing, Inc.: Raleigh, NC, USA, 2004.
18. Knott, E.F. *Radar Cross Section Measurements*; Van Nostrand Reinhold: New York, NY, USA, 2012.
19. Drake, V.A.; Chapman, J.W.; Lim, K.S.; Reynolds, D.R.; Riley, J.R.; Smith, A.D. Ventral-aspect radar cross sections and polarization patterns of insects at X band and their relation to size and form. *Int. J. Remote Sens.* **2017**, *38*, 5022–5044. [CrossRef]
20. Bakker, F.T.; Antonelli, A.; Clarke, J.A.; Cook, J.A.; Edwards, S.V.; Ericson, P.G.; Faurby, S.; Ferrand, N.; Gelang, M.; Gillespie, R.G.; et al. The Global Museum: Natural history collections and the future of evolutionary science and public education. *PeerJ* **2020**, *8*, e8225. [CrossRef]

21. Hedrick, B.P.; Heberling, J.M.; Meineke, E.K.; Turner, K.G.; Grassa, C.J.; Park, D.S.; Kennedy, J.; Clarke, J.; Cook, J.; Blackburn, D.C.; et al. Digitization and the Future of Natural History Collections. *BioScience* **2020**, *70*, 243–251. [CrossRef]
22. Balke, M.; Schmidt, S.; Hausmann, A.; Toussaint, E.F.; Bergsten, J.; Buffington, M.; Häuser, C.L.; Kroupa, A.; Hagedorn, G.; Riedel, A.; et al. Biodiversity into your hands—A call for a virtual global natural history 'metacollection'. *Front. Zool.* **2013**, *10*, 55. [CrossRef]
23. Waring, P.; Townsend, M. *Field Guide to the Moths of Great Britain and Ireland*, 3rd ed.; Bloomsbury: London, UK, 2017.
24. Feng, H.; Wu, X.; Wu, B.; Wu, K. Seasonal Migration of *Helicoverpa armigera* (Lepidoptera: *Noctuidae*) Over the Bohai Sea. *J. Econ. Entomol.* **2009**, *102*, 95–104. [CrossRef]
25. Feng, H.Q.; Zhao, X.C.; Wu, X.F.; Wu, B.; Wu, K.M.; Cheng, D.F.; Guo, Y.Y. Autumn Migration of *Mythimna Separata* (Lepidoptera: *Noctuidae*) over the Bohai Sea in Northern China. *Environ. Entomol.* **2008**, *37*, 774–781. [CrossRef]
26. Westbrook, J.K. Noctuid migration in Texas within the nocturnal aeroecological boundary layer. *Integr. Comp. Biol.* **2008**, *48*, 99–106. [CrossRef] [PubMed]
27. Li, C.; Fu, X.; Feng, H.; Ali, A.; Li, C.; Wu, K. Seasonal Migration of *Ctenoplusia agnata* (Lepidoptera: *Noctuidae*) Over the Bohai Sea in Northern China. *J. Econ. Entomol.* **2014**, *107*, 1003–1008. [CrossRef] [PubMed]
28. Fu, X.; Feng, H.; Liu, Z.; Wu, K. Trans-regional migration of the beet armyworm, *Spodoptera exigua* (Lepidoptera: *Noctuidae*), in North-East Asia. *PLoS ONE* **2017**, *12*, e0183582. [CrossRef] [PubMed]
29. Westbrook, J.; Eyster, R. Doppler weather radar detects emigratory flights of noctuids during a major pest outbreak. *Remote Sens. Appl. Soc. Environ.* **2017**, *8*, 64–70. [CrossRef]
30. Fu, X.; Zhao, X.; Xie, B.; Ali, A.; Wu, K. Seasonal Pattern of *Spodoptera litura* (Lepidoptera: *Noctuidae*) Migration across the Bohai Strait in Northern China. *J. Econ. Entomol.* **2015**, *108*, 525–538. [CrossRef] [PubMed]
31. Wood, C.; Reynolds, D.; Wells, P.; Barlow, J.; Woiwod, I.; Chapman, J. Flight periodicity and the vertical distribution of high-altitude moth migration over southern Britain. *Bull. Entomol. Res.* **2009**, *99*, 525–535. [CrossRef]
32. Wood, C.R.; Chapman, J.W.; Reynolds, D.R.; Barlow, J.F.; Smith, A.D.; Woiwod, I.P. The influence of the atmospheric boundary layer on nocturnal layers of noctuids and other moths migrating over southern Britain. *Int. J. Biometeorol.* **2006**, *50*, 193–204. [CrossRef]
33. Chapman, J.W.; Lim, K.S.; Reynolds, D.R. The significance of midsummer movements of Autographa gamma: Implications for a mechanistic understanding of orientation behavior in a migrant moth. *Curr. Zool.* **2013**, *59*, 360–370. [CrossRef]
34. Chapman, J.W.; Reynolds, D.; Mouritsen, H.; Hill, J.K.; Riley, J.R.; Sivell, D.; Smith, A.D.; Woiwod, I.P. Wind Selection and Drift Compensation Optimize Migratory Pathways in a High-Flying Moth. *Curr. Biol.* **2008**, *18*, 514–518. [CrossRef]
35. NBN Atlas. Available online: https://species.nbnatlas.org/species/NHMSYS0021144939#overview (accessed on 3 October 2020).
36. Fedorov, A.; Beichel, R.; Kalpathy-Cramer, J.; Finet, J.; Fillion-Robin, J.-C.; Pujol, S.; Bauer, C.; Jennings, D.; Fennessy, F.; Sonka, M.; et al. 3D Slicer as an image computing platform for the Quantitative Imaging Network. *Magn. Reson. Imaging* **2012**, *30*, 1323–1341. [CrossRef]
37. Blender Online Community. *Blender—A 3D Modelling and Rendering Package*; Stichting Blender Foundation: Amsterdam, The Netherlands, 2018.
38. Denning, J.; Lampel, J.; Williamson, J.; Moore, P.; Crawford, P.; Gearhart, C. Retopoflow: A Suite of Retopology Tools for Blender through a Unified Retopology Mode. Version 3.0, Beta 2. 2020. Available online: https://github.com/CGCookie/retopoflow (accessed on 3 October 2020).
39. Wasserthal, L.T. Respiratory System. In *Handbook of Zoology: Lepidoptera, Moths and Butterflies*; Kristensen, N.P., Ed.; De Gruyter: Berlin, Germany, 2003; Volume 4/36-2, pp. 189–203.
40. Simelane, S.M.; Abelman, S.; Duncan, F.D. Gas Exchange Models for a Flexible Insect Tracheal System. *Acta Biotheor.* **2016**, *64*, 161–196. [CrossRef] [PubMed]
41. Kolundzija, B.M. Electromagnetic modeling of composite metallic and dielectric structures. *IEEE Trans. Microw. Theory Tech.* **1999**, *47*, 1021–1032. [CrossRef]
42. Kolundzija, B.; Ognjanovic, J.; Sarkar, T.; Harrington, R. WIPL: A program for electromagnetic modeling of composite-wire and plate structures. *IEEE Antennas Propag. Mag.* **1996**, *38*, 75–79. [CrossRef]
43. Smith, A.; Reynolds, D.; Riley, J. The use of vertical-looking radar to continuously monitor the insect fauna flying at altitude over southern England. *Bull. Entomol. Res.* **2000**, *90*, 265–277. [CrossRef] [PubMed]
44. Drake, V. Signal processing for ZLC-configuration insect-monitoring radars: Yields and sample biases. In Proceedings of the International Conference on Radar IEEE, Adelaide, Australia, 9–12 September 2013; pp. 298–303. [CrossRef]
45. Drake, V.A. Distinguishing target classes in observations from vertically pointing entomological radars. *Int. J. Remote Sens.* **2016**, *37*, 3811–3835. [CrossRef]
46. Nelson, S.O.; Bartley, P.G., Jr.; Lawrence, K.C. RF and microwave dielectric properties of stored-grain insects and their implications for potential insect control. *Trans. ASAE* **1998**, *41*, 685–692. [CrossRef]
47. Dorsett, D.A. Preparation for Flight by Hawk-Moths. *J. Exp. Biol.* **1962**, *39*, 579–588. [CrossRef]
48. Heath, J.E.; Adams, P.A. Regulation of Heat Production by Large Moths. *J. Exp. Biol.* **1967**, *47*, 21–33. [CrossRef]
49. Bartholomew, G.A.; Heinrich, B. A Field Study of Flight Temperatures in Moths in Relation to Body Weight and Wing Loading. *J. Exp. Biol.* **1973**, *58*, 123–135. [CrossRef]

50. Chen, H.; Li, X.; Yu, W.; Wang, J.; Shi, Z.; Xiong, C.; Yang, Q. Chitin/MoS_2 Nanosheet Dielectric Composite Films with Significantly Enhanced Discharge Energy Density and Efficiency. *Biomacromolecules* **2020**, *21*, 2929–2937. [CrossRef]
51. Chapman, J.; Reynolds, D.; Smith, A.; Smith, E.; Woiwod, I. An aerial netting study of insects migrating at high altitude over England. *Bull. Entomol. Res.* **2004**, *94*, 123–136. [CrossRef]
52. Sane, S.P. The aerodynamics of insect flight. *J. Exp. Biol.* **2003**, *206*, 4191–4208. [CrossRef] [PubMed]
53. Aiello, B.R.; Bin Sikandar, U.; Minoguchi, H.; Bhinderwala, B.; Hamilton, C.A.; Kawahara, A.Y.; Sponberg, S. The evolution of two distinct strategies of moth flight. *J. R. Soc. Interface* **2021**, *18*, 20210632. [CrossRef] [PubMed]
54. Andryieuski, A.; Kuznetsova, S.M.; Zhukovsky, S.V.; Kivshar, Y.S.; Lavrinenko, A.V. Water: Promising Opportunities for Tunable All-dielectric Electromagnetic Metamaterials. *Sci. Rep.* **2015**, *5*, 13535. [CrossRef]
55. Kong, S.; Hu, C.; Wang, R.; Zhang, F.; Wang, L.; Long, T.; Wu, K. Insect Multifrequency Polarimetric Radar Cross Section: Experimental Results and Analysis. *IEEE Trans. Geosci. Remote Sens.* **2021**, *59*, 6573–6585. [CrossRef]
56. Truett, G.; Heeger, P.; Mynatt, R.; Truett, A.; Walker, J.; Warman, M. Preparation of PCR-Quality Mouse Genomic DNA with Hot Sodium Hydroxide and Tris (HotSHOT). *BioTechniques* **2000**, *29*, 52–54. [CrossRef] [PubMed]
57. Folmer, O.; Black, M.; Hoeh, W.; Lutz, R.; Vrijenhoek, R. DNA primers for amplification of mitochondrial cytochrome c oxidase subunit I from diverse metazoan invertebrates. *Mol. Mar. Biol. Biotechnol.* **1994**, *3*, 294–299.
58. Hajibabaei, M.; Janzen, D.H.; Burns, J.M.; Hallwachs, W.; Hebert, P.D.N. DNA barcodes distinguish species of tropical Lepidoptera. *Proc. Natl. Acad. Sci. USA* **2006**, *103*, 968–971. [CrossRef]